

A DESKTOP COMPUTER MODEL OF ARC WELDING USING A CFD APPROACH

Anthony B. MURPHY^{1*}, David G. THOMAS², Vu NGUYEN³, Yuqing FENG⁴ and Dayalan GUNASEGARAM³

¹ CSIRO Manufacturing, Lindfield, NSW 2070, AUSTRALIA

² CSIRO Data 61, Clayton, Victoria 3169, AUSTRALIA

³ CSIRO Manufacturing, Clayton, Victoria 3169, AUSTRALIA

⁴ CSIRO Minerals Resources, Clayton, Victoria 3169, AUSTRALIA

*Corresponding author, E-mail address: tony.murphy@csiro.au

ABSTRACT

A sophisticated computational model of metal–inert gas arc welding of aluminium is presented. The arc plasma, the electrode and the workpiece are included in the computational domain self-consistently. The flow in the arc plasma and in the weld pool are calculated in three dimensions using equations of computational fluid dynamics, modified to take into account plasma effects and coupled to electromagnetic equations. A graphical user interface has been developed, and the model runs on standard desktop or laptop computers.

The computational model is described, and results are presented for lap fillet weld geometry. The importance of including the arc in the computational domain is shown. The predictions of the model are compared to measurements of weld geometry and weld composition. The GUI is introduced, and the application of the model to predicting the thermal history of the workpiece, which is the input information that is required for predicting important weld properties such as residual stress and distortion and weld microstructure, is discussed.

NOMENCLATURE

A magnetic potential
B magnetic field strength
 c_p specific heat at constant pressure
 D_d^l self-diffusion coefficient of liquid metal
 e electronic charge
g gravitational acceleration
 h specific enthalpy
 h_M specific enthalpy of metal vapour
 h_S specific enthalpy of shielding gas
 I arc current
j current density
 j_e electron current density
 \mathbf{J}_M diffusion mass flux of metal vapour
 k thermal conductivity
 k_B Boltzmann's constant
 P pressure
 P_a pressure on arc side of arc–workpiece interface
 P_w pressure on workpiece side of interface
 r_e wire electrode radius
 S_d droplet alloy source term
 S_M metal vapour mass source term
 S_{vap} latent heat of vapourisation source term
 T temperature

U net radiative emission coefficient
 \mathbf{v} velocity
 \mathbf{V} welding velocity
 V_i ionisation energy of shielding gas
 x_i coordinates in three-dimensional geometry
 x_{\parallel} displacement parallel to top of workpiece
 x_{\perp} displacement perpendicular to top of workpiece
 Y_d mass fraction of droplet alloy
 Y_M mass fraction of metal vapour
 ϕ electric potential
 ϕ_w work function of workpiece material
 γ surface tension of weld pool
 η dynamic viscosity
 κ surface curvature of weld pool
 μ_0 permittivity of free space
 ρ mass density
 σ electrical conductivity
 σ_e electrical conductivity at the top of the wire electrode
 $\boldsymbol{\tau}$ stress tensor
 τ_a shear stress on arc side of arc–workpiece interface
 τ_w shear stress on workpiece side of interface

INTRODUCTION

Arc welding is a process that is used very widely in manufacturing and other industries. The most widely used type of arc welding in manufacturing industry is metal–inert-gas (MIG) welding, which is known as metal–active-gas (MAG) welding when oxygen or carbon dioxide is added to the inert shielding gas. MIG and MAG welding are also known collectively as gas–metal arc welding (GMAW). In MIG/MAG welding, an arc plasma is struck between a wire electrode and the metal parts that are being joined, which are known as the workpiece. The energy transferred by the arc partially melts the workpiece, forming the weld pool. The wire electrode melts, forming droplets that pass through the arc into the weld pool.

In this paper, we present a three-dimensional computational model of MIG welding of aluminium. The development of the model was motivated by the increasing use of aluminium in the automotive industry, and the fact that aluminium is more difficult to weld than steel. A need therefore exists for a computational tool to assist welding engineers in designing weld schedules to join particular components. To help meet this need, a graphical user interface (GUI) has been developed to allow easy use of

the computer code. The code runs under 64-bit Windows on any desktop or laptop computer with 6 GB of RAM.

MODEL DESCRIPTION

Unlike most arc welding models, the arc plasma, the electrode and the workpiece, including the weld pool, are all included in the computational domain self-consistently (i.e., there is two-way coupling between the different regions). The equations to be solved are those for viscous incompressible flow of a non-isothermal fluid, with modifications to account for the conduction of electricity and effects specific to a plasma. Most of the equations have been given previously (Murphy, 2011; Murphy, 2013a), and are presented here for completeness.

The mass continuity equation is:

$$\nabla \cdot (\rho \mathbf{v}) = S_M, \quad (1)$$

where the source term on the right-hand side describes production of metal vapour from the electrode and workpiece. The equation of momentum conservation is:

$$\nabla \cdot [\rho(\mathbf{v} - \mathbf{V})(\mathbf{v} - \mathbf{V})] = -\nabla P - \nabla \cdot \boldsymbol{\tau} + \mathbf{j} \times \mathbf{B} + \rho \mathbf{g}. \quad (2)$$

The terms on the right-hand side describe respectively the forces due to pressure gradients, viscous stress, the Lorentz or magnetic pinch force, and gravity. The stress tensor is given in Cartesian geometry by

$$\begin{aligned} \tau_{ii} &= \eta \left(2 \frac{\partial v_i}{\partial x_i} - \frac{2}{3} \nabla \cdot \mathbf{v} \right), \\ \tau_{ij} &= \eta \left(\frac{\partial v_i}{\partial x_j} + \frac{\partial v_j}{\partial x_i} \right), \quad i \neq j. \end{aligned} \quad (3)$$

The equation of energy conservation is

$$\begin{aligned} \nabla \cdot [\rho(\mathbf{v} - \mathbf{V})h] &= \frac{\mathbf{j}^2}{\sigma} - \nabla \cdot \left(\frac{k}{c_p} \nabla h \right) \\ -\nabla \cdot \left[(h_M - h_S) \frac{k}{c_p} \nabla Y_M \right] &- \frac{5k_B}{2ec_p} \mathbf{j} \cdot \nabla h - U - S_{\text{vap}}. \end{aligned} \quad (4)$$

The terms on the right-hand side describe respectively resistive heating, thermal conduction, change of enthalpy due to the mixing of metal vapour and the argon shielding gas, energy transfer arising from the flow of electrons, radiative emission and the latent heat of vaporisation, which is non-zero only at the boundaries between the plasma and liquid metal. The enthalpy is the integral of specific heat with respect to temperature, and the temperature at any position is easily derived from the enthalpy at that position. Equations (2) and (3) are transformed into the frame of reference of the wire electrode, which moves at velocity \mathbf{V} with respect to the fixed workpiece.

The equation of current continuity is

$$\nabla \cdot \mathbf{j} = \nabla \cdot (\sigma \nabla \phi) = 0. \quad (5)$$

The magnetic field strength \mathbf{B} , which appears in equation (2), also has to be calculated. This can be done by using $\mathbf{B} = \nabla \times \mathbf{A}$ and solving for the magnetic potential \mathbf{A} :

$$\nabla^2 \mathbf{A} = -\mu_0 \mathbf{j}. \quad (6)$$

Metal vapour, produced chiefly from the molten tip of the wire electrode, but also from the droplets and weld pool,

strongly influences the properties of the arc. The rate of vaporisation of the electrode and weld pool is calculated self-consistently using the Hertz–Langmuir equation and depends on the local temperature of the wire electrode or weld pool surface and the mass fraction of the vapour in the adjacent plasma. Modelling of the diffusion of the metal vapour required an additional conservation equation, for the mass fraction of metal species (atoms, ions and the electrons derived from metal atoms):

$$\nabla \cdot (\rho \mathbf{v} Y_M) = -\nabla \cdot \mathbf{J}_M = S_M. \quad (7)$$

The diffusion mass flux \mathbf{J}_M was calculated using the combined diffusion coefficient method, which is equivalent to the full multicomponent approach (Murphy, 1993).

The wire and the workpiece are generally composed of different alloys. The droplets formed from the wire pass into the weld pool, so the two alloys become mixed. To take this into account, it is necessary to solve an additional conservation equation, for the mass fraction Y_d of the droplet alloy:

$$\nabla \cdot (\rho \mathbf{v} Y_d) = -\nabla \cdot (\rho D_d' \nabla Y_d) + S_d. \quad (8)$$

The equations are solved in three-dimensional Cartesian geometry, using the finite volume method of Patankar (1980), incorporating the SIMPLEC algorithm of van Doormaal and Raithby (1984).

The latent heat of melting at the liquid–solid interfaces is treated using the method of Voller et al. (1989). The shape of the free surface between the weld pool and the arc is calculated by minimising the total surface energy of the liquid metal, using the approach presented by Kim and Na (1995). This method takes into account the surface tension and surface curvature, the arc and droplet pressure, buoyancy in the weld pool, and the volume of metal transferred to the weld pool by droplets.

A time-averaged treatment of the influence of the droplets was developed (Murphy, 2013b); this treatment is computationally much faster than the volume-of-fluids method, but still allows the influence of the droplets on the arc plasma and the weld pool to be determined. The temperature, velocity and diameter of the droplets are tracked from their detachment from the wire to their impact with the weld pool, with the heat, momentum and mass transfer determined using the methods of Crowe et al. (1977). The effect of the droplets on the plasma and weld pool are included using source terms averaged over the spatial extent of the droplet path and time. The method has the drawback that changes in the shape of the tip of the wire as droplets form and detach are not considered.

Boundary Conditions

A cross-section of the computational domain is shown in Figure 1. The temperature at the external boundaries is set to 300 K, except for the plane at the bottom of the workpiece, for which a heat flux boundary condition is used. The velocity components are zero at the boundaries of the gaseous region, except for a small region at the top boundary, where inflow through a nozzle is simulated. The pressure needs only to be defined at one point; it is set to 1 atm at the top corner. The electric potential is set to zero at the bottom of the workpiece, and its gradient at the

top of the wire electrode is given by $\partial\phi/\partial z = I/(\pi\sigma_e r_e^2)$.

Metal vapour mass fractions have constant gradients at the edge of the gaseous region.

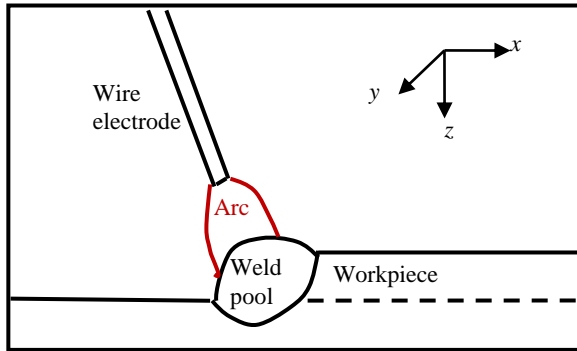


Figure 1: Schematic showing a cross section of the computational domain.

The boundary conditions at the internal boundaries between the electrodes and plasma have to be treated carefully. Four physical factors are important in determining the influence of the arc plasma on the weld pool: the heat flux, the current density, the shear stress, and the arc pressure, all at the weld pool surface.

The workpiece is a non-thermionic cathode, for which the electron emission mechanism is not well understood. We use the following expressions for the heat flux (Lowke and Tanaka, 2008):

$$S = j_e (V_i - \phi_w) - k \partial T / \partial x_{\perp}. \quad (9)$$

The first term describes heating due to electron flux, and the second due to thermal conduction. The boundary conditions for momentum transfer across the arc–weld-pool interface parallel and perpendicular to the weld pool surface are respectively

$$\begin{aligned} \tau_a - \tau_w + (d\gamma/dT)(dT/dx_{\parallel}) + (d\gamma/dY_d)(dY_d/dx_{\parallel}) &= 0, \\ P_a - P_w + \gamma\kappa &= 0. \end{aligned} \quad (10)$$

The parallel boundary condition states that the difference in shear stress across the interface is determined by the Marangoni term $d\gamma/dx_{\parallel}$, which describes the variation of the surface tension due to the gradients of temperature and composition close to the weld pool surface. The perpendicular boundary condition states that the pressure difference across the interface is determined by the product of the surface tension and the curvature.

The top electrode is a metal wire anode, for which the heat transfer boundary condition is given by

$$S = j_e \phi_w - k \partial T / \partial x_{\perp}. \quad (11)$$

Again, the first term describes heating due to electron flux, and the second due to thermal conduction.

Thermophysical Properties

The thermophysical properties of the shielding gases, such as thermal conductivity and electrical conductivity, were taken from Murphy and Arundell (1994) for argon, with properties for mixtures of argon and aluminium vapour calculated as described by Murphy (2010). Net radiative

emission coefficients for argon were taken from Cram (1985) and for aluminium from Essoltani et al. (1994), with data for mixtures calculated based on mole fractions as recommended by Gleizes et al. (2010).

The calculations presented here were performed for a workpiece composed of aluminium alloy AA5754, and for an AA4043 wire. AA5754 was assumed to have the composition Al + 3.1 wt% Mg, and AA4043 Al + 5.3 wt% Si. Since mixing of the wire and workpiece alloy was considered, the thermophysical properties of intermediate mixtures had to be determined. An analysis of literature data was undertaken to determine the properties of liquid and solid mixtures of Al with Mg and Si.

PREDICTIONS OF THE MODEL

Calculations were performed for welding parameters typical for those used for sheet aluminium in the automotive industry. Lap fillet weld geometry (i.e., two workpiece sheets, with one partially covering the other, as shown in Figure 1) was used. The power supply operates in one-drop-per-pulse mode, with a pulsed current increase used to detach droplets at a predetermined frequency. The parameters are given in Table 1. The travel angle is the angle of the wire electrode from the horizontal in the y - z plane, and the work angle is its angle from the horizontal in the x - z plane.

Parameter	Value
Arc current (average)	95 A
Shielding gas	Argon, 14 L/min
Distance from wire tip to workpiece (without reinforcement)	5 mm
Welding speed	0.9 m/min (15 mm/s) in $-y$ direction
Wire diameter	1.2 mm
Wire feed rate	4.32 m/min (72 mm/s)
Droplet frequency	93 Hz
Work angle	60°
Travel angle	90°
Wire alloy	AA 4043 (Al + 5.3 wt% Si)
Workpiece thickness (each sheet)	3 mm
Workpiece alloy	AA 5754 (Al + 3.1 wt% Mg)
Workpiece orientation	Horizontal

Table 1: Parameters used in calculations

The temperature and current density distributions in the wire, arc and workpiece, and the distributions of flow speed and aluminium vapour mass fraction in the arc, are shown in Figure 2. The temperature of the arc reaches 11 900 K just below the wire. There is another region of high temperature close to where the arc attaches to the workpiece. The temperature in the weld pool reaches the boiling point of aluminium (2723 K) near this point. The arc temperature is substantially below that predicted and measured for a pure argon arc; this is due to both the stronger radiative emission from aluminium vapour, and the cooling due the flux of relatively cool metal vapour into the arc from the wire tip (Murphy, 2013a).

The current density in the arc is largest close to the points at which the arc attaches to the wire and workpiece, as is expected. There are two main attachment regions at the workpiece, a larger region from $x = -0.2$ mm to $+1.8$ mm,

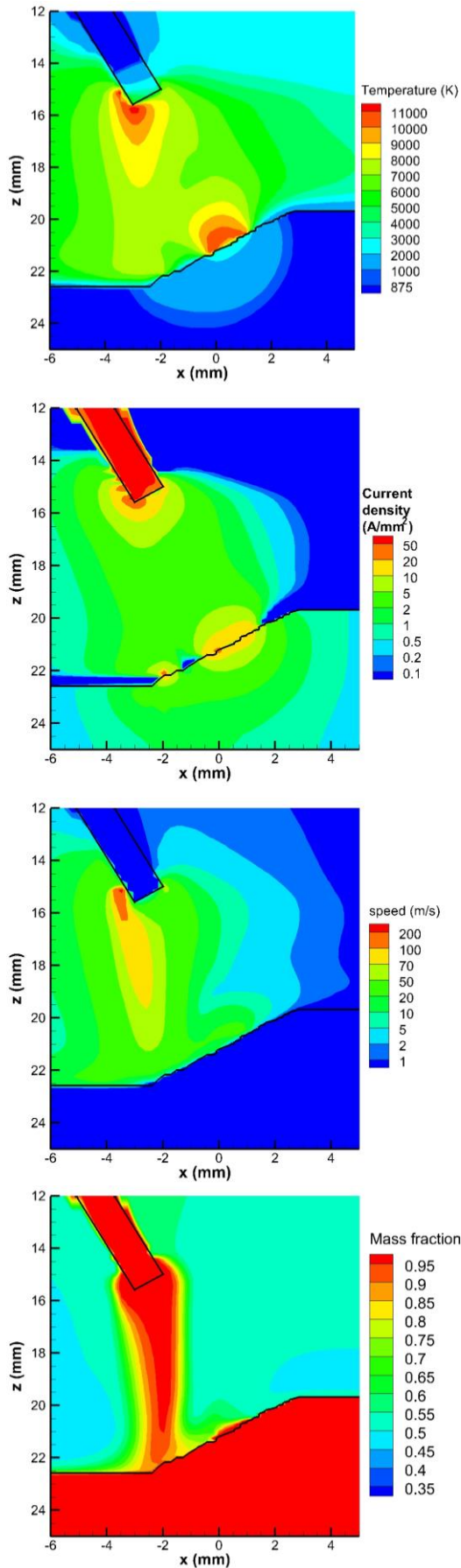


Figure 2: Distributions of temperature, current density, flow speed and aluminium vapour mass fraction in the vertical plane through the wire electrode.

adjacent to the region of highest temperature in the weld pool, and a smaller region at $x = -2$ mm, vertically below the wire. These regions have high metal vapour concentrations. The metal vapour in the larger attachment region is produced from the weld pool, while that in the smaller region is produced from the wire and advected downwards by the plasma flow. The metal vapour mass fraction is predicted to be very high, at least 0.9, in the region below the wire. The vapour is calculated to be produced from the wire at a rate of 4.4 mg/s, corresponding to about 2% of the wire mass feed rate (the remainder of the wire is converted to droplets).

The distributions of temperature and current density close to the workpiece determine the heat transfer to the workpiece, according to equation (9). The distributions are complicated, and depend on both the profile of the weld pool surface and the metal vapour distribution in the arc. This demonstrates the importance of including the arc in the computational domain. If the arc is instead represented by a boundary condition at the workpiece surface, the free parameters in the expression describing the arc have to be fitted to measurements, and this process has to be repeated for every significant change in welding parameters.

The flow in the weld pool depends on the momentum transferred by the droplets, the Marangoni effect (arising from the dependence of surface tension on temperature and composition), the magnetic pinch force and buoyancy. In previous work, we have shown that droplet momentum and magnetic pinch force are the dominant mechanisms in MIG welding of aluminium (Murphy, 2013b).

Figure 3 shows the mixing of the droplet into the weld pool, with both the distribution of the droplet alloy and the flow vectors given. The flow is strongly downwards at the position of droplet impact. The droplet alloy follows the flow vectors in the weld pool. Eventually, the complex flow patterns, and diffusive mixing, lead to the droplet and workpiece alloys becoming better mixed.

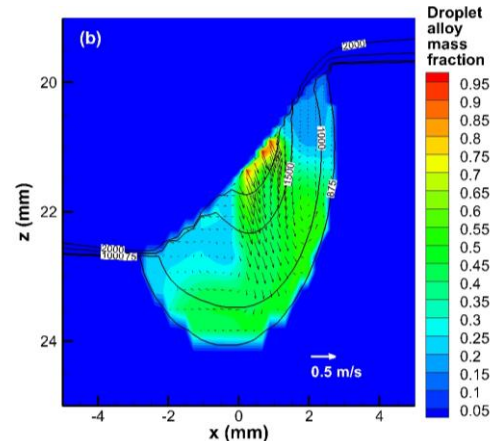


Figure 3: Fraction of the droplet alloy in a cross-section of the weld pool, for the $y = 0.2$ mm plane. Velocity vectors, and temperature contours for 875, 1000, 1500 and 2000 K are also shown.

COMPARISON WITH EXPERIMENT

Measurements of the weld cross-section were performed by welding aluminium sheets along a straight line for at least 200 mm. After cooling, the plate was cut at

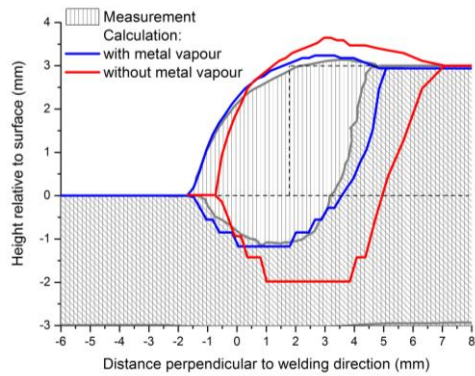


Figure 4: Comparison of measured weld cross-sections with those predicted by the computational model. Predictions of the model including and excluding the influence of metal vapour are shown. The original metal profile is shown by the broken line. The parameters are as given in Table 1, except for arc current 104 A, welding speed 10 mm s⁻¹ and wire feed rate 78 mm s⁻¹.

approximately the midpoint of the welded section. The measured weld cross-section is compared in Figure 4 to that predicted by the computational model, both including and neglecting the production of metal vapour.

When metal vapour is neglected, the computational model predicts that the weld pool is much larger than indicated by the measurements. When metal vapour is considered, the weld pool is shallower, in good agreement with the measured depth and shape. There are two main reasons for the decrease of the weld pool depth. The first is that the arc temperature is lower, so the conductive heat flux to the workpiece is smaller. The second is that the current density at the upper surface of the workpiece is lower, owing to the increased electrical conductivity of the arc plasma at lower temperatures, which leads to a spreading of the arc attachment regions (Murphy, 2013a).

Figure 5 shows a comparison between the silicon distribution in a weld cross-section, measured using an FEG-EPMA (field emission gun – electron probe microanalyser) on a scanning electron microscope, and the predicted droplet alloy distribution. Since the wire electrode, and therefore the droplets, contain Si, and the workpiece does not, the two images should approximately correspond. The predictions agree qualitatively with the measurements, with relatively large concentrations of Si near the bottom left of the weld cross section, and lowest concentrations of Si near the left-hand top and centre top of the weld cross section.

GRAPHICAL USER INTERFACE

To allow the model to be used by engineers and technicians unfamiliar with computational modelling, a graphical user interface (GUI) has been developed. This allows the user to select welding parameters (arc current, welding speed, wire feed rate, droplet frequency, shielding gas flow rate), geometric parameters (weld geometry, wire diameter, workpiece sheet thicknesses, work and travel angles of the wire, arc length), and the alloys used for the wire and workpiece. One of the parameter input windows is shown in Figure 6.

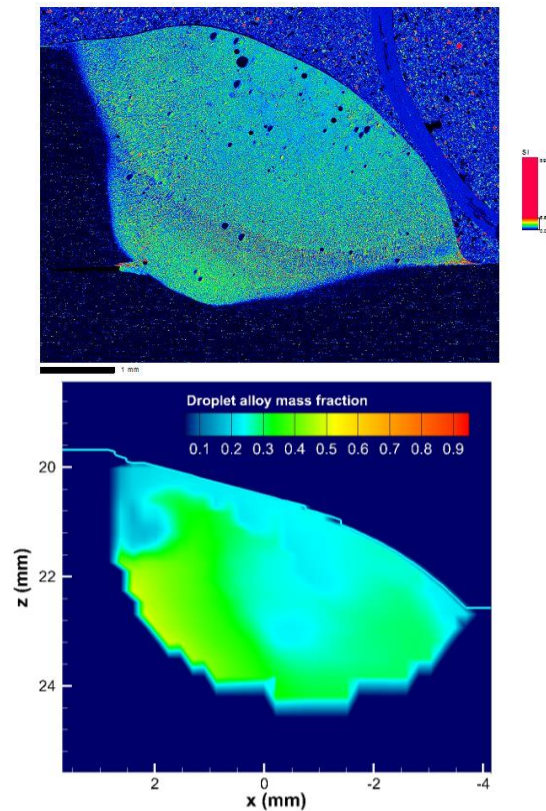


Figure 5: Measured silicon mass fraction in a cross-section of the weld (top) and calculated mass fraction of the droplet alloy (bottom). The scale in the top image runs from 0% Si (black) to 6.6% Si (red).

Once the required parameters are entered, the computation can be started and convergence monitored. When the computation is complete, graphical representations of the weld pool, workpiece and arc properties can be viewed.

The model runs on any 64-bit personal computer under Windows, with each iteration taking less than 30 s on a four-processor machine. Depending on the chosen parameters, several tens to several hundreds of iterations are required for convergence.

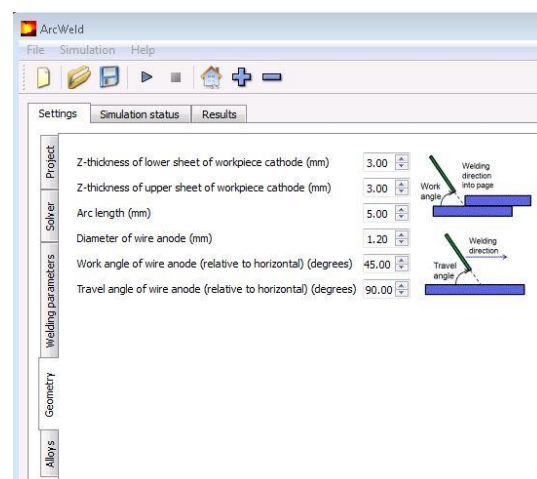


Figure 6: View of the graphical user interface, showing the geometry input window.

FUTURE DIRECTIONS

The weld depth and shape are of critical importance in arc welding. Nevertheless, there are several other factors that are often of similar importance. These include the residual stress in, and consequent deformation of, the welded metal, and the microstructure of the metal in the solidified weld pool and the broader heat-affected zone. Both these properties affect the in-service reliability of the weld.

The computational model that has been presented here allows prediction of the thermal histories at every point in the workpiece. An example is shown in Figure 7. These are the input data required for models that predict residual stress and deformation, and microstructure, of the welded metal. Coupling the arc welding model to such residual stress and microstructure models will allow accurate prediction of these properties over a wide parameter range.

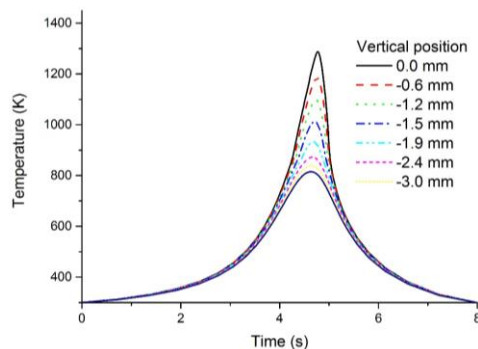


Figure 7: Thermal history at different vertical (z) positions at $x = 0$. The x and z coordinates correspond to those used in Figure 4.

The model presented here could be extended to allow the treatment of a greater range of MIG welding parameters, including the use of active shielding gases, welding of metals such as steels and titanium, and multi-pass welding. There is scope to incorporate optimisation algorithms to assist in determining optimum welding parameters. It would also be feasible to adapt the model to related processes such as arc additive manufacturing.

CONCLUSIONS

A computational model of MIG welding of aluminium has been developed. Using a GUI, it is possible to run the model on standard desktop and laptop computers. The model allows prediction of weld depth and shape, and distributions of temperature, velocity and current density in the arc and weld pool, metal vapour in the arc, and droplet alloy in the weld pool. The predictions of the model show good agreement with measurements of weld cross sections and droplet alloy distribution.

An important advantage of including the arc in the computational domain, is that the welding parameters can be varied without requiring recalibration of the boundary conditions. This is in contrast to conventional models, in which the arc is only represented as boundary conditions on the top surface of the workpiece. Such models require recalibration of the free parameters in the boundary conditions whenever the welding parameters are varied.

Using thermal histories of the welded metal predicted by our model, it will be possible to predict the residual stress

and the microstructure of the metal. This in turn will allow assessment of the regions most vulnerable to damage, and the in-service durability of the weld.

ACKNOWLEDGEMENTS

The support provided for the work reported here by General Motors, General Motors Holden, and the Commonwealth of Australia, through the AutoCRC, is gratefully acknowledged. Drs John Lowke and Eugene Tam of CSIRO and Dr Hui-Ping Wang of General Motors are thanked for useful discussions, and Mr Colin MacRae of CSIRO for performing the FEG-EPMA measurements.

REFERENCES

- CRAM, L.E., (1985), "Statistical evaluation of radiative power losses from thermal plasmas due to spectral lines", *J. Phys. D: Appl. Phys.*, **18**, 401-411.
- CROWE, C.T., SHARMA, M.P. and STOCK, D.E., (1977), "The particle-source-in cell (PSI-CELL) model for gas-droplet flows", *J. Fluid. Eng.*, **99**, 325-332.
- ESSOLTANI, A., PROULX, P., BOULOS, M.I. and GLEIZES, A., (1994), "Volumetric emission of argon plasmas in the presence of vapors of Fe, Si and Al", *Plasma Chem. Plasma Process.*, **14**, 437-450.
- GLEIZES, A., CRESSAULT, Y. and TEULET, P., (2010), "Mixing rules for thermal plasma properties in mixtures of argon, air and metallic vapours", *Plasma Sources Sci. Technol.*, **19**, 055013.
- KIM, J.-W. and NA, S.-J., (1995), "A study on the effect of contact tube-to-workpiece distance on weld pool shape in gas metal arc welding", *Weld. J.*, **74**, 141s-152s.
- LOWKE, J.J. and TANAKA, M. (2008), "The physics of non-thermionic cathodes of electric arcs", *Proc. 17th International Conference on Gas Discharges and their Applications*, Cardiff, Wales, pp. 137-140.
- MURPHY, A.B., (1993), "Diffusion in equilibrium mixtures of ionized gases", *Phys. Rev. E*, **48**, 3594-3603.
- MURPHY, A.B., (2010), "The effects of metal vapour in arc welding", *J. Phys. D: Appl. Phys.*, **43**, 434001.
- MURPHY, A.B., (2011), "A self-consistent three-dimensional model of the arc, electrode and weld pool in gas-metal arc welding", *J. Phys. D: Appl. Phys.*, **44**, 194009.
- MURPHY, A.B., (2013a), "Influence of metal vapour on arc temperatures in gas-metal arc welding: convection versus radiation", *J. Phys. D: Appl. Phys.*, **46**, 224004.
- MURPHY, A.B., (2013b), "Influence of droplets in gas-metal arc welding – a new modelling approach, and application to welding of aluminium", *Sci. Technol. Weld. Join.*, **18**, 32-37.
- MURPHY, A.B. and ARUNDELL, C.J., (1994), "Transport coefficients of argon, nitrogen, oxygen, argon-nitrogen and argon-oxygen plasmas", *Plasma Chem. Plasma Process.*, **14**, 451-490.
- PATANKAR, S.V., (1980), "Numerical Heat Transfer and Fluid Flow", Hemisphere, Washington DC.
- VAN DOORMAL, J.P. and RAITHBY, G.D., (1984), "Enhancements of the SIMPLE method for predicting incompressible fluid flows", *Numer. Heat Transfer*, **7**, 147-163.
- VOLLER, V.R., BRENT, A.D. and PRAKASH, C., (1989), "The modelling of heat, mass and solute transport in solidification systems", *Int. J. Heat Mass Transfer*, **32**, 1719-1731.